

Simulations of Silicon-on-Insulator Channel-Waveguide Electrooptical 2×2 Switches and 1×1 Modulators Using a $\text{Ge}_2\text{Sb}_2\text{Te}_5$ Self-Holding Layer

Haibo Liang, Richard Soref, *Life Fellow, IEEE*, Jianwei Mu, *Member, IEEE*, Arka Majumdar, *Member, IEEE*, Xun Li, *Senior Member, IEEE*, and Wei-Ping Huang, *Senior Member, IEEE*

Abstract—This paper reports theoretical designs and simulations of electrooptical 2×2 switches and 1×1 loss modulators based upon GST-embedded SOI channel waveguides. It is assumed that the amorphous and crystalline phases of GST can be triggered electrically by Joule heating current applied to a 10-nm GST film sandwiched between doped-Si waveguide strips. TE_0 and TM_0 mode effective indices are calculated over 1.3 to 2.1- μm wavelength range. For 2×2 Mach-Zehnder and directional coupler switches, low insertion loss, low crosstalk, and short device lengths are predicted for 2.1 μm , although a decreased performance is projected for 1.55 μm . For 1.3–2.1 μm , the 1×1 EO waveguide has application as a variable optical attenuator and as a digital modulator, albeit with ≤ 100 -ns state-transition time. Because the active material has two “stable” phases, the device holds itself in either state, and voltage needs to be applied only during transition.

Index Terms—Electrooptic devices, modulators, optical switches, optical waveguide, phase change materials.

I. INTRODUCTION

THE phase-change material $\text{Ge}_2\text{Sb}_2\text{Te}_5$, commonly known as GST, is reported to have optical response superior to that of the other opto-electronically interesting phase-change material vanadium dioxide (VO_2) [1]. New applications are emerging in electrically controlled GST film for free-space optical filters and in GST film-loaded optical waveguides controlled

Manuscript received October 13, 2014; revised January 2, 2015 and December 3, 2014; accepted January 9, 2015. Date of publication January 14, 2015; date of current version March 13, 2015. The work of H. Liang was supported by NSERC under the SiEPIC CREATE program. The work of R. Soref was supported by the Air Force Office of Scientific Research (Dr. G. Pomrenke) under Grant FA9550-14-1-0196 and by the U.K. EPSRC through the Project entitled MIGRATION. The work of A. Majumdar was supported by the startup fund provided by the UW, Seattle.

H. Liang and X. Li are with the Department of Electrical and Computer Engineering, Mc Master University, Hamilton L8S 4L8, Canada (e-mail: liangh3@mcmaster.ca; lixun@mcmaster.ca).

R. Soref is with the Physics Department and the Engineering Program, University of Massachusetts at Boston, Boston, MA 02125 USA (e-mail: soref@rcn.com).

J. Mu was with the Microphotonics Center and the Department of Materials Science and Engineering, Massachusetts Institute of Technology, Cambridge, MA 02139 USA (e-mail: mujw@mit.edu).

A. Majumdar is with the Department of Electrical Engineering, University of Washington, Seattle, WA 98195 USA (e-mail: arka.majumdar@gmail.com).

W.-P. Huang is with the School of Information Science and Engineering, Shandong University, Jinan 250100, China (e-mail: wphuang_canada@hotmail.com).

Color versions of one or more of the figures in this paper are available online at <http://ieeexplore.ieee.org>.

Digital Object Identifier 10.1109/JLT.2015.2393293

optically by an external 700-nm light beam [2]–[4]. We, however, consider electrical control to be more suitable for practical applications than the optical actuation. The thrust of this paper is to combine electrical control with optical waveguiding by embedding a thin GST film between doped silicon waveguide strips in order to provide two useful transmission states for the channel waveguide. Those two self-sustaining states correspond to the amorphous and crystalline phases of GST. The resulting electro-optical (EO) devices are analyzed in this paper using electro-magnetic modeling to predict the responses of the fundamental TE and TM guided modes in the near- and mid-infrared wavelength bands. The $1 \times 10^{18} \text{ cm}^{-3}$ P- or N-type doping proposed here provides adequate electrical contact to the film for Joule-heated phase change but does not decrease significantly the optical transparency of the waveguide.

The organization of this paper is as follows. EO structures for 2×2 spatial routing (switching) and 1×1 modulations are proposed. The complex refractive indexes $n + ik$ for both the amorphous and crystalline phases of GST in the 1000–2400-nm wavelength range are compiled via an extensive literature survey. Reliable index values are found for estimating switch and loss-modulator performance in several silicon-based structures wherein a localized “ribbon segment” of GST buried in Si or Ge serves as the active length of the modulator or switch. The substrate is assumed to be CMOS-compatible silicon-on-insulator (SOI). We also examined a photonic slot in the channel comprised of 1.96-index indium-tin oxide (ITO) and we considered the effect of two GST layers. The TE and TM behaviors are simulated and from that we determined spectral regions for switching and for step-wise modulation.

II. PROPOSED WAVEGUIDES FOR SWITCHES, MODULATORS AND VARIABLE OPTICAL ATTENUATOR (VOA)

The recent experiments of Hosseini *et al.* [5] presented a convincing demonstration of electrically induced phase change in a 7-nm film of GST phase change material (PCM). This layer was contacted above and below by doped ITO layers that provided electrical connection to the terminals of a voltage source. That source drove current pulses through the “resistive” PCM. The resulting Joule heating of GST transformed its phase as desired for optical applications: in fact, the ITO was optically transparent at the wavelengths of interest as desired for EO uses. In the

present paper, we assumed that: (1) doped semiconductor layers or doped ITO layers contact the upper and lower surfaces of the GST film, (2) voltage across those layers is able to induce the desired thermal phase change via Joule heating current, and (3) the doped waveguiding materials are adequately transparent in the near/mid infrared for high transmission through the waveguide. What is proposed here is lightwave propagation in the plane of the GST layer as opposed to the normal-incidence transmission through the film used by Hosseini *et al.* [5]. Because of multi-micron travel in the film plane, the guided mode here “senses” the GST complex index and responds to changes in index.

Experiments in the literature [2], [3] have placed GST upon an exposed surface of a waveguide where this GST layer acts as optical cladding so as to effect the relatively weak “fringing field” of the guided mode [6], [7]. Those papers demonstrated modulation and switching by means of a “pumping” light beam incident upon the cladding. The design presented here is new in two ways: (1) the thin film is placed midway in the body of the waveguide where it has a much stronger effect upon the mode indices; (2) the phase change—rather than being optically triggered—is electrically induced. We are not aware of any prior art on EO GST-core waveguides. A third new aspect of the present work is that we utilize both the electro-refraction (ER) and the electro-absorption (EA) component of the induced phase change. Another innovation here—in the context of EO waveguides—is the “latching” or self-holding feature. Regarding prior electrical drive, there was a report of sandwiching VO_2 within a metallic “plasmonic” slot [6]. Also, a multi-micron length of VO_2 cladding was resistance-heated [7]. However, we are not aware of any EO prior art in a PCM photonic-waveguide core.

In the present work, the GST indices are consistently higher than those of the silicon waveguide body; hence the GST layer forms an “anti-slot” within the waveguide. The simulations detailed below have yielded new behavior of the anti-slot, not anticipated. Unexpectedly, the TE-polarized light is particularly sensitive to the induced change of GST complex index $\Delta n + i\Delta k$, more so than in TM. Unexpectedly, the ratio $\Delta n/\Delta k$ is consistently higher in TM than TE. The loss suppression in TM indicates that ER dominates in TM. Thus, with the anti-slot, TM is more favorable for low-loss 2×2 switching, whereas TE is the most natural mode polarization for 1×1 EA applications. We discovered a waveguide size effect in which a large cross-section increased the TM confinement. As mentioned, these findings were not expected. We have also examined the effect of thin GST layers that are placed adjacent to an ITO “photonic slot” introduced into the silicon channel, and have studied symmetric and asymmetric cladding of the channel with SiO_2 . Germanium was substituted for silicon in the waveguide and similar responses were found.

Our specific proposal for constructing the EO waveguide is illustrated in Fig. 1 where an active GST waveguide “segment” is end-fire coupled into and out of a uniform undoped channel waveguide. The SOI approach is selected in order to make this structure manufacturable and compatible with the silicon “CMOS photonics” industry. This device could also be germanium-on-insulator for wavelengths longer than $1.8 \mu\text{m}$.

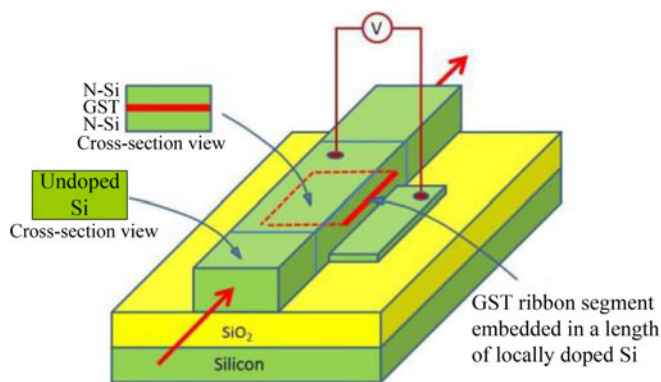


Fig. 1. Perspective view of proposed 1×1 SOI EO channel waveguide modulator employing a wavelength-scale segment of “buried” GST ultrathin ribbon.

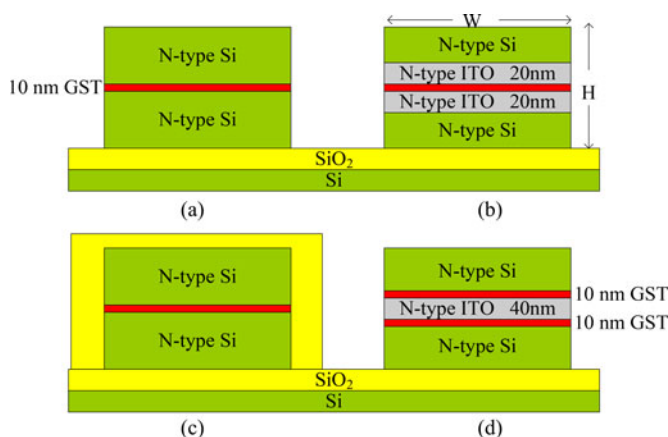


Fig. 2. Cross-section view of four SOI EO waveguide structures investigated.

The Fig. 1 insets, the cross sections, show the smooth transition between the undoped passive-channel sections and the doped active section. Insertion of the EO region in this manner is expected to offer low insertion loss (IL) because of good mode matching and low reflections between passive and active segments. Such low IL is anticipated for both TE and TM. We investigated four approaches to layering thin-film GST within the channel as illustrated in the cross-sectional views of Fig. 2. In the simplest case, GST is inserted at the mid-plane of the channel (see Fig. 2(a)). Here the GST would be sputter-deposited in the amorphous phase on a half-channel crystalline strip of doped silicon, after which a second half-channel strip of dense polycrystalline silicon, suitably doped, would be grown upon the GST. A bonded nano-membrane approach is an alternative fabrication technique.

In Fig. 2(a), the channel rests on the SiO_2 -coated Si substrate with three sides of the channel exposed to air, whereas in Fig. 2(c) this channel is clad all-around by SiO_2 . A second EO method is a five-layer technique: the GST is sandwiched between two very thin layers of doped ITO where this ITO/GST/ITO is located at mid channel, and the ITO/GST/ITO is sandwiched between doped silicon layers to form Si/ITO/GST/ITO/Si (see Fig. 2(b)). In effect, this

produces two photonic slots related to the hybrid plasmonic slot explored by other groups [8], [9]. A third way is a two-GST approach for making the EO waveguide (see Fig. 2(d)) wherein a single photonic slot is created. Electrically, the Fig. 2 multi-layers amount to several “resistors” connected in series, a path that brings current to the resistive GST. Note that the device is not a diode as usually employed in conventional silicon photonic modulators. The electrical equivalent circuits in the above examples are either three resistors or five resistors. Layer thicknesses must be chosen for good optical performance. In terms of optical field concentrations, Fig. 2(a) and (c) are anti-slot, whereas (b) contains two photonic slots, while (d) offers one slot. All four versions can be incorporated in Fig. 1.

III. ELECTRICALLY INDUCED PHASE CHANGE

In this section, we shall consider the waveguide fabrication processes and shall “prove” from a theoretical standpoint that the proposed structures can work properly. Regarding the Fig. 2 waveguide layering, when the top Si film is deposited on ITO or on GST, that silicon will be polycrystalline. This does not present a problem for two reasons: (1) the real index and the loss factor of N-doped poly Si are quite close to those of N-doped crystal Si, (2) the poly-Si can be readily N-doped to $\sim 10^{18} \text{ cm}^{-3}$ in order to attain an electrical conductivity that is sufficient to drive GST.

We considered the SiO_2 -embedded Si/GST/Si waveguide for the $2.1 \mu\text{m}$ wavelength (10-nm GST, 205-nm doped-Si stripes). There are two related thermal procedures: re-crystallization from the amorphous phase to the crystalline phase, and the reverse— from the crystalline phase to the amorphous phase.

In detail, the recrystallization requires an applied set voltage pulse of 100-ns duration as in [10] that induces temperature rise above 413 K [11] but below 819 K (the melting point) [12]. The conductivity of GST in an initial amorphous state is small (0.1 S/m [15]), and without “stimulation” it is impossible to launch enough current to heat the layer to melting. However, when the electric field component of the applied voltage pulse is larger than a “threshold value”, then the GST becomes conductive with no phase change [15]. To simulate re-crystallization, we assume that the applied field is above threshold, that the material starts to recrystallize, and that the GST conductivity has an average value of 1000 S/m during the 100-ns set time [10]. The actual process is more complex because the conductivity increases during “set” and the heating process is accelerated. Using COMSOL software, we simulated the temperature rise induced by a 5 V set pulse applied for 100 ns ($E = 50 \text{ V}/\mu\text{m}$). Taking into account the thermal and electrical resistance circuits and the resulting current and electric power dissipation, the modeling yields the spatial distribution and time dependence of temperature rise. Here we found that the current density finally reached $2.17 \text{ A}/\text{m}^2$ and the GST temperature rose to 420 K in average during this time interval as required for recrystallization.

As for the changing process from crystalline to amorphous state, a shorter reset voltage pulse of typically 1 to 10 ns duration is employed, and there the GST film temperature must be raised above the melting point and then quenched rapidly by

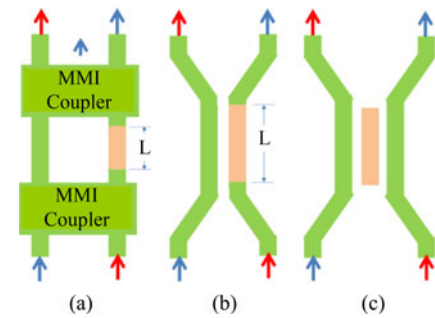


Fig. 3. Top view of proposed non-resonant 2×2 SOI EO channel waveguide spatial routing switches: (a) MZI, (b) two-waveguide directional coupler, and (c) three-waveguide directional coupler. The orange-shaded region indicates an embedded electrically addressed GST ribbon segment.

the pulse falling to zero in $< 1 \text{ ns}$. This required annealing of the film is discussed in [14]. In our simulation, a 15 V pulse was applied for 2 ns to the waveguided crystal GST having $2770 \text{ S}/\text{m}$ conductivity [13], and here the result was a current density of $6.7 \text{ A}/\text{m}^2$ induced in GST. This produced a very strong temperature rise $\sim 980 \text{ K}$ in the film (above the 891 K as desired). In reality, after this “brief” melting, the latent heat of molten GST ($1.37 \times 10^5 \text{ J}/\text{kg}$ [15]) will consume most of the input power, pinning the temperature to the melting point and protecting the contact material. In summary, the electrically switched waveguide is indicated to work properly. The voltages that we applied in both simulations might be considered as “relatively high”; however, this is a trade-off we are willing to make to achieve optimum optical performances in the coming sections.

IV. PERFORMANCE GUIDELINES FOR 2×2 SWITCHES

Fig. 3 shows the layout of three proposed 2×2 switches with the GST EO segment shaded in orange where its active length is L . Each device has self-holding “cross” and “bar” states, states 1 and 2 that correspond to the two phases of GST. In each of its phases, the GST has a complex index of refraction, and the optical waveguide performance is linked to a change in both the real and imaginary indices. We can quantify optical performance using some definitions of indices and absorption. The GST indices are written for the amorphous phase $n_{\text{am}} + ik_{\text{am}} = n_1 + ik_1$, and for the crystalline phase $n_{\text{cr}} + ik_{\text{cr}} = n_2 + ik_2$, while the channel waveguide has a mode effective index in each state written as $n_{1e} + ik_{1e}$ and $n_{2e} + ik_{2e}$. Looking at the extinction coefficient k , let us denote α as the absorption loss of the waveguide in decibel per micrometer in each state, $\alpha = 4.34(4\pi k/\lambda)$. The IL of an amorphous active waveguide of length L is proportional to the product αL , that is $IL \text{ (dB)} = 4.34(4\pi k_{1e}L/\lambda)$ and the crystalline-phase loss is $4.34(4\pi k_{2e}L/\lambda)$. The extinction ratio of a loss modulator discussed below is then $ER \text{ (dB)} = (k_{2e} - k_{1e})(4.34)(4\pi L/\lambda)$. The Fig. 1 waveguide combines strong $n_{2e} - n_{1e}$ ER with strong $k_{2e} - k_{1e}$ EA because there are significant swings in both real and imaginary GST indices induced by change of phase. By choosing the wavelength of operation appropriately, either the ER or EA component can be emphasized. Loss modulation utilizes EA, while ER is mostly

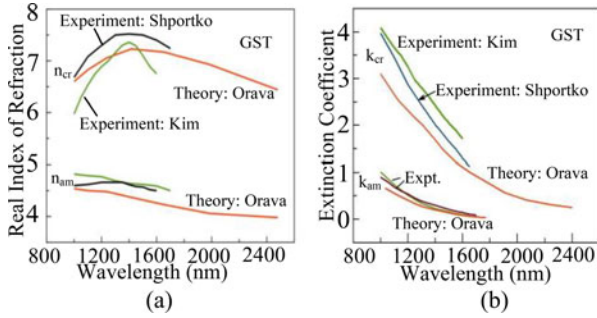


Fig. 4. Wavelength dependence of: (a) the real and (b) the imaginary refractive index components of GST (both phases) as replotted from literature sources.

neglected: 2×2 switching relies upon ER, with additional requirements that: (1) $ER \gg EA$, and (2) absorption loss in the initial cross state is low. For spatial routing switches, EA and initial loss are “side effects” that must be worked with to keep high performance.

In switches, it is the product of the phase factor $\Delta\beta$ with L , that affects the transfer of light from the input guide to the output guide, where $\Delta\beta L = (2\pi/\lambda)(n_{2e} - n_{1e})$. Values of $\Delta\beta L$ from 3 to 18 are required, depending upon the switch geometry [16] and upon whether the device is resonant or non-resonant. Specifically, in Fig. 3, the Mach–Zehnder interferometer (MZI) requires $\Delta\beta L = \pi$ rad, while the two-waveguide directional coupler needs $\Delta\beta L = 5.4$ rad, and the three-waveguide directional coupler requires $\Delta\beta L = 18$ rad. To minimize IL and crosstalk (CT) in both switching states, we generally desire $n_{2e} - n_{1e} \gg k_{2e} - k_{1e}$ with the ratio $\rho = (n_{2e} - n_{1e})/(k_{2e} - k_{1e})$ being as high as possible. Because the IL of the initial switch state is proportional to the $k_{1e}L$ product, a “moderate” value of k_{1e} can present a loss problem when $L > 50\lambda$. Since k_{1e} is λ -dependent, then λ must be chosen to give minimization of k_{1e} together with maximization of $n_{2e} - n_{1e}$. This happens at longer wavelengths. In cases where non-resonant switches do not provide an adequate combination of low- IL low- CT effective indices, then the resonant versions of those switching devices would give satisfactory performance in side-coupled nano-beams [17] and in a bus-ring-ring-bus structure [18].

V. GST REFRACTIVE INDICES VERSUS WAVELENGTH

Before simulations can be started, it is necessary to have reliable values of the complex indices $n + ik$ of GST. Literature sources of n and k are discussed in this section as a basis for waveguide modeling. Partially crystallized or “fractional” intermediate states are not considered; only the amorphous and the rocksalt-structured crystal phases are examined. The four indices n_{am} , k_{am} , n_{cr} , k_{cr} have been plotted in various literature reports as a function of wavelength or of photon energy. Reports are given by Kim *et al.* [19, Fig. 1], Orava *et al.* [20, Fig. 4], Gholipour *et al.* [21, Fig. 2(b)], Yamada [22, Fig. 10.10] which was taken from Strand’s data [23], and from Choi [24] which is based upon the experimental ϵ_1 and ϵ_2 permittivity measurements of Shportko *et al.* [see 25, Fig. 4]. Choi deduced n and k from ϵ_1 and ϵ_2 out to 1650 nm. Regarding n_{am} and n_{cr} , there is good agreement among the literature reports, except for the

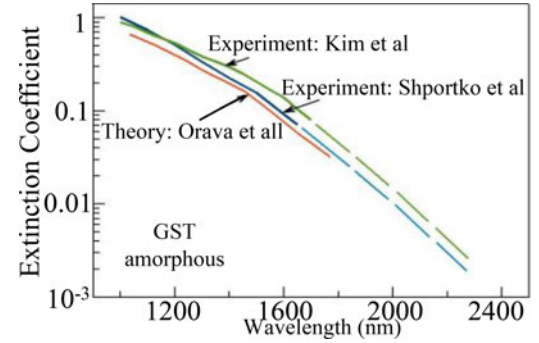


Fig. 5. Semi-log plot of the extinction-coefficient dispersion of GST’s amorphous phase.

TABLE I
VALUES OF THE n AND k INDICES THAT WERE UTILIZED IN THE PRESENT SIMULATIONS

Material	$\lambda = 1310$ nm		$\lambda = 1550$ nm		$\lambda = 2100$ nm	
	n	k	n	k	n	k
GST(Amorphous)	4.68	0.33	4.60	0.12	4.05	0.006
GST(Crystal)	7.51	2.38	7.45	1.49	6.80	0.40
N-Silicon	3.50	0.0001	3.48	0.0002	3.45	0.0003
N-Germanium	—	—	—	—	4.09	0.0003
N-ITO	0.96	0.002	1.94	0.002	1.92	0.003
Silicon Dioxide	1.45	0.0	1.44	0.0	1.44	0.0

data of Gholipour which is systematically lower. That GST data requires a scale factor of 1.6 to bring it into concordance with other reports. In Fig. 4(a), we have plotted for the 1000–2400 nm region Orava’s theory curves for n_{am} and n_{cr} . Also, the measured data points of Kim and of Shportko in the 1000–1600 nm range have been replotted in this Fig. 4(a). Note that, due to the non-stoichiometric nature of GST, the experimental properties of GST depend strongly upon the details of fabrication.

Next we considered the loss values of k_{am} and k_{cr} . The 2×2 switching relies upon k_{am} being very small, and that constraint rules out wavelengths below 1600 nm because only beyond that wavelength does k_{am} fall significantly; hence 1600–2400 nm is prime for switching, whereas 1×1 loss modulation can use both k values over 1310–2400 nm. In Fig. 4(b) we have replotted the k_{am} , k_{cr} experimental results of Kim and of Shportko along with the theory calculations of Orava. The experimental n_{am} , n_{cr} , k_{am} , k_{cr} curves of Strand *et al.* [23] verify Orava’s 1600–2400 nm theory curves in Fig. 4(a) and (b). To supplement the information in Fig. 4(b), we note that Tsuda *et al.* [26] presented experimental results at the specific wavelength of 1550 nm and their report of $n_1 + ik_1 = 4.39 - i0.16$, $n_2 + ik_2 = 7.25 - i1.55$ is in close agreement with the measurements of Shportko *et al.* [25], which are $n_1 + ik_1 = 4.60 - i0.12$, $n_2 + ik_2 = 7.45 - i1.49$. We elected to use the Shportko values for 1550 and 1310 nm. In the literature, k_{am} becomes very small at wavelengths beyond 1.6 μm and that behavior has not yet been quantified. Because knowledge of k_{am} has relevance to MIR switching, we examined in detail the 1000–2200 nm range. First, in the semi-log plot of Fig. 5, we plotted in 1000-to-1650 nm the measured k_{am} values.

TABLE II
SIMULATION RESULTS FOR THE FIG. 2(A) WAVEGUIDES

Geometry	Claddings	λ (nm)	$W \times H$ (nm)	Mode	Δn_e	Δk_e	ρ	α_{1e} (dB/ μ m)	α_{2e} (dB/ μ m)	$\alpha_{2e} - \alpha_{1e}$ (dB/ μ m)
SGS	3 air 1 oxide	1310	524x262	TE(TM)	0.248(0.039)	0.355(0.006)	0.700(6.704)	1.166(0.314)	15.923(0.555)	14.757(0.240)
		1550	620x310	TE(TM)	0.255(0.031)	0.190(0.005)	1.341(5.906)	0.302(0.090)	6.990(0.274)	6.687(0.183)
		2100	840x420	TE(TM)	0.17(0.027)	0.033(0.002)	5.179(15.311)	0.015(0.012)	0.879(0.058)	0.864(0.045)

Next we extrapolated those curves to 2200 nm as indicated by the dashed lines in Fig. 5. In addition, we show the calculated values of k_{am} going out to 2200 nm. There is special interest in switching near 2000 nm because a new generation of hollow-core photonic bandgap fibers is being developed for operation in the 1900 to 2100 nm wavelength band [27] and such fiber transmission is central to increasing the information capacity of global fiber-optic networks. For applying EO switching in this communications context, we considered the GST loss in Fig. 5 in the 2000-nm region where k_{am} is decreasing rapidly. We selected $\lambda = 2100$ nm as being a compromise between missing the fiber-loss valley and attaining the lowest k_{am} . At 2100 nm, we elected to use the extrapolation from Shportko data for consistency with the choices in Fig. 4(a) and (b). Specifically $k_{am} = 0.006$. For the other index values k_{cr} , n_{am} , and n_{cr} at 2100 nm we turned to the theory of Orava.

The index values for doped ITO, Si, and Ge were estimated as follows. The N-doping of Si at $1 \times 10^{18} \text{ cm}^{-3}$ density produces k values in the $1-3 \times 10^{-4}$ range according to [28]. For N-Ge having the same donor concentration as N-Si, the k at 2100 nm is 0.003 according to unpublished estimates of M. Nedeljkovic at the University of Southampton. For N-type ITO, a doping level of $5 \times 10^{18} \text{ cm}^{-3}$ was assumed. Then the size of both n and k in the $1.31-2.1 \mu\text{m}$ range was determined by scaling the 10^{19} cm^{-3} N-ITO index data presented in Huang *et al.* [29]. All of the index values used in the simulations are tabulated in Table I.

We close this section by considering the potential for high performance 2×2 and $N \times N$ switching across the $2-5 \mu\text{m}$ wavelength span. Beyond $3 \mu\text{m}$, the SiO_2 cladding in Fig. 1 becomes absorbing and can be replaced easily by transparent Si_3N_4 . For GST, Shportko's data [25] show that the index difference $n_{cr} - n_{am}$ stays quite high over $2-5 \mu\text{m}$ while both k_{cr} and k_{am} decline dramatically since the photon energy is below the respective bandgap energies. We do not know whether [25] takes into account free-carrier effects in the crystalline phase that could cause k_{cr} to rise up near $5 \mu\text{m}$. If k_{cr} indeed remains negligible, then the GST 2×2 figure-of-merit actually increases in the $2-5 \mu\text{m}$ range.

VI. RESULTS OF NUMERICAL SIMULATIONS

In all simulations, we have taken the GST thickness as 10 nm for good electrical and optical performance. ITO thickness is given in Fig. 2. We calculated the complex effective index of the fundamental TE or TM mode at the wavelengths 1310, 1550 and 2100 nm using the COMSOL software. Regarding the $W \times H$ waveguide cross section, our first simulations utilized the

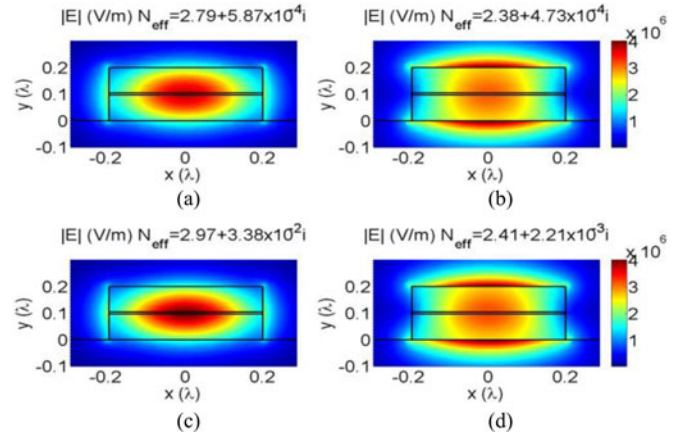


Fig. 6. Mode distribution for SGS waveguide at $\lambda = 2100$ nm. (a) TE, amorphous. (b) TM, amorphous. (c) TE, crystal. (d) TM, crystal.

$500 \text{ nm} \times 250 \text{ nm}$ dimensions usually adopted in the Si photonics industry for 1550-nm single-mode SOI channels. Although the mode confinement was very good for TE in Fig. 2(a), we quickly found that the TM-polarization mode confinement in Fig. 2(a) was problematic because TM-mode energy leaked out of the Si strips in the vertical direction and gave considerable mode tailing into the substrate and air claddings. Empirically we found that employing W and H dimensions about 25% larger gave much better TM confinement. That is why we used $W = 0.4\lambda$ and $H = 0.2\lambda$ throughout the rest of the simulations reported here.

Results for the first group of simulations performed for Fig. 2(a) are tabulated in Table II, where we list the changes in effective index, the ratio ρ , and the effective-index loss in decibel per micrometer for both the first and the second states. The term SGS is used to denote Si/GST/Si.

The detailed mode profile over the X - Y cross-section was determined and representative results at the 2100 nm wavelength are given in Fig. 6. The mode patterns for 1310 and 1550 nm (not shown) are quite similar to the 2100-nm pattern. The next group of simulations was for the slotted-GST waveguides of Fig. 2(b), where SIGIS denotes Si/ITO/GST/ITO/Si. Here we present the complete results in Table III. Representing graphically the Table III results at 2100 nm, the TE and TM mode profiles shown in Fig. 7 indicate that the TM mode is now bunching in the slot, concentrating more at mid-region than in Fig. 6, while the induced index changes in Table III are not much different than those found in Table II. The final group of results pertains to Fig. 2(c) and (d) where we examine an all-around symmetric cladding and a double-GST EO layer that sandwiches an ITO photonic slot, while the GST/ITO/GST is sandwiched in

TABLE III
SIMULATION RESULTS FOR THE FIG. 2(B) WAVEGUIDES

Geometry	Claddings	λ (nm)	$W \times H$ (nm)	Mode	Δn_e	Δk_e	ρ	α_{1e} (dB/ μ m)	α_{2e} (dB/ μ m)	$\alpha_{2e} - \alpha_{1e}$ (dB/ μ m)
SIGIS	3 air 1 oxide	1310	524x 262	TE(TM)	0.212(0.015)	0.317(0.005)	0.667(3.336)	1.024(0.176)	14.236(0.365)	13.212(0.189)
		1550	620x 310	TE(TM)	0.225(0.014)	0.171(0.005)	1.315(3.020)	0.273(0.074)	6.287(0.233)	6.015(0.159)
		2100	840x 420	TE(TM)	0.155(0.015)	0.030(0.001)	5.147(11.724)	0.020(0.037)	0.803(0.070)	0.783(0.033)

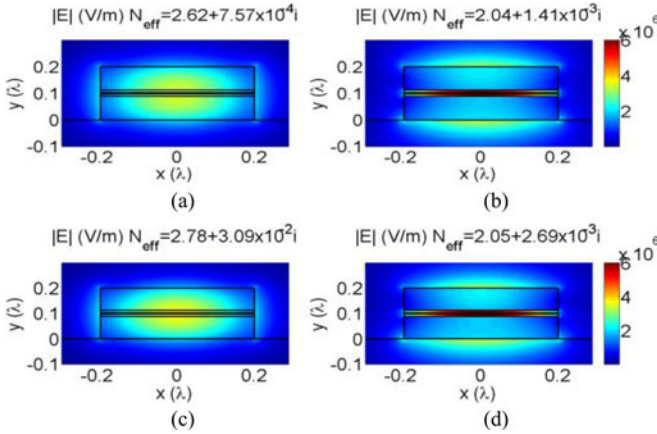


Fig. 7. Mode distribution for the Fig. 2(b) SIGIS waveguide at $\lambda = 2100$ nm. (a) TE, amorphous. (b) TM, amorphous. (c) TE, crystal. (d) TM, crystal.

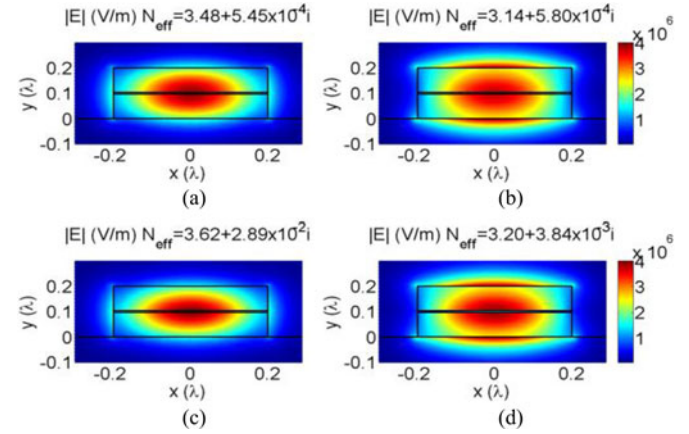


Fig. 9. Mode distribution for the Ge/GST/Ge waveguides at $\lambda = 2100$ nm. (a) TE, amorphous. (b) TM, amorphous. (c) TE, crystal. (d) TM, crystal.

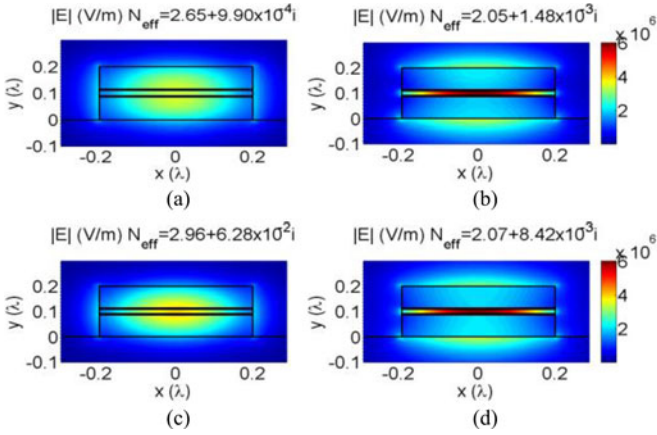


Fig. 8. Mode distribution for the SGIS waveguides at $\lambda = 2100$ nm. (a) TE, amorphous. (b) TM, amorphous. (c) TE, crystal. (d) TM, crystal.

Si. This Si/GST/ITO/GST/Si layering is termed SGIGS. A final simulation looked at substituting Ge for Si in Fig. 2(a). Results for these cases are summarized in Table IV. The mode profiles for the double-GST-with-slot and for the Ge waveguide case are presented in Figs. 8 and 9. The TE and TM profiles for the all-around oxide cladding are not shown because they exhibit little change in mode distribution compared to that of air-clad.

VII. PREDICTED 2×2 SWITCHING PERFORMANCE

As per Tables III and IV, the introduction of multiple layers does not elevate significantly the Δn and Δk performance found in Table II, and so we shall use the TM SGS results in Table II to estimate switching performance at 1550 and 2100 nm for the

devices of Fig. 4(a) and (b), with the $\Delta\beta L$ of 3.14 and 5.4 rad, respectively, in the bar state. These $\Delta\beta$ conditions allow us to find L in the bar state, a length that also becomes the cross-coupling length L . After that we can estimate the initial cross state IL as $\alpha_{1e}L$. For the MZI, we turn to [16, Fig. 2] to determine IL and CT in the bar state. Then for the two-waveguide coupler, we utilize [16, Fig. 8] in order to estimate IL and CT in the bar state. The complete results are summarized in Table V where 2WGDC is the two-waveguide directional coupler.

Looking at these Table V estimates, the TM performance generally is very good at 2100 nm as discussed below, but is problematic for GST at 1550 nm because of the rather high IL in the MZI cross and bar states and in the 2WGDC cross state. Now we shall highlight an application of TE switching. Moving now from the 2WGDC to the three-waveguide device of Fig. 3(c) at 2100 nm, we can compare the switching performance obtained using the TE mode with the performance given by the TM mode. Table II shows that $\rho(\text{TE})$ unfortunately decreases by 66% relative to $\rho(\text{TM})$; however Δn_e (TE) is $6.4 \times$ larger than that of $\Delta n_e(\text{TM})$ while $\alpha_{1e}(\text{TE})$ increases by only $1.3 \times$ over $\alpha_{1e}(\text{TM})$. These properties can be used to good advantage in the Fig. 3(c) three-waveguide coupler. There the TE mode can be used to attain a significantly decreased cross-state IL at the expense of an increased bar-state IL . Turning to germanium-on-insulator, the TM-mode Ge 2×2 switches will, it appears, work quite well at 2100 nm. The photonic-slot TM devices, both SIGIS and SGIGS, have generally lower ρ values, implying decreased performance relative to SGS.

Returning to Table V, we can compare the expected performance of GST-enabled switches to state-of-the-art 2×2 EO devices in the SOI silicon photonics art. Starting with the

TABLE IV
SIMULATION RESULTS FOR THE FIG. 2(C) AND (D) WAVEGUIDES AS WELL AS GERMANIUM IN FIG. 2(A)

Geometry	Claddings	λ (nm)	WxH (nm)	Mode	Δn_e	Δk_e	ρ	α_{1e} (dB/ μ m)	α_{2e} (dB/ μ m)	$\alpha_{2e} - \alpha_{1e}$ (dB/ μ m)
SGS	4 oxide	2100	840 \times 420	TE(TM)	0.167(0.025)	0.032(0.002)	5.160(16.038)	0.015(0.012)	0.856(0.053)	0.841(0.041)
SGIGS	3 air 1 oxide			TE(TM)	0.317(0.029)	0.062(0.007)	5.136(4.202)	0.026(0.039)	1.631(0.219)	1.605(0.180)
GeGGe	3 air 1 oxide			TE(TM)	0.147(0.052)	0.028(0.002)	5.178(15.878)	0.014(0.015)	0.751(0.100)	0.736(0.085)

TABLE V
ESTIMATED AND SIMULATED PERFORMANCES OF 2×2 SWITCHES USING THE TM-POLARIZED ACTIVE SGS SEGMENT

λ (nm)	PCM	MZI L (μ m)	MZI Cross IL(am) dB	MZI Cross CT(am) dB	MZI Bar IL(cr) dB	MIZ Bar CT(cr) dB	2WGDC L (μ m)	2WGDC Cross IL(am) dB	2WGDC Cross CT(am) dB	2WGDC Bar IL(cr) dB	2WGDC Bar CT(cr) dB
1550	GST	25	2.3	-15	3.4	-9.9	43	3.9	-15	1.0	-17
2100	GST	38	0.5	-15	1.1	-16	67	0.8	-15	0.4	-22

2WGDC, we searched the literature but were not able to locate any experimental coupler examples, recent or early, in the electro-optic SOI art. However, the theory of Soref [16] indicates that an SOI PIN-injected 2WGDC at $\lambda = 2100$ nm would have an active length of 614 μ m as compared to the $L = 67$ μ m in Table V. There are many experimental 2×2 MZI reference switch examples in the recent 1550-nm SOI electro-optic literature. Since there are no literature results for our preferred wavelength of 2100 nm, we shall use an extrapolation of the recent test results reported at 1550 nm [see 30, Fig. 2(c)] in which a lateral PIN-diode strongly injected free carriers into a 200- μ m active Si length. That MZI device attained IL (cross) = 0.2 dB and CT (cross) = -15 dB as well as IL (bar) = 1.0 dB and CT (bar) = -20 dB. That device would presumably work *just as well* at 2100 nm. Then, Table V indicates that our $L = 38$ - μ m switch has quite comparable IL and CT performance.

Regarding speed, there are “set” and “reset” times needed for “electrical” phase transition. The largest time is around 100 ns according to [5] which would limit the modulation speed in a digital return-to-zero format to around 0.5 Mb/s if we assume that the bit duration is $10 \times$ longer than a 100-ns transition time. This modulation rate is slightly faster than that available in thermo-optic effect modulators, but is surely much slower than that in free-carrier-effect modulators. Regarding energy, we have not attempted here to quantify the energy consumption of the modulator. However, we see that energy is consumed only during the state transitions, and no energy is consumed to maintain a state. Packet switching or message switching is often used in $N \times N$ routing switches, and there the <100 ns re-configuration would usually be adequate.

VIII. PREDICTED 1×1 MODULATOR AND VOA PERFORMANCE

The principal devices are illustrated in Fig. 10. It is evident from an inspection of Tables II, III and IV that the TE mode offers very strong and practical EA over the entire 1.31–2.1 μ m range. TM has some EA utility but at a lower on/off attenuation ratio. The designer of the 1×1 loss-modulated device has a variety of parameters from which to choose. Along with the

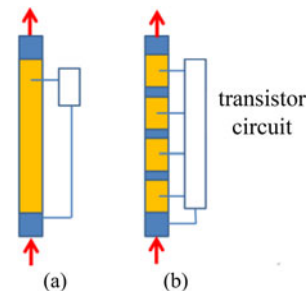


Fig. 10. Top view, schematic, of 1×1 EO waveguide (a) loss modulator, (b) VOA with discretized control.

wavelength, the mode polarization, the cladding geometry and the materials layering can be chosen. Those selections lead to a particular α_{1e} determined in the relevant table above. Then the active length L can be chosen to provide a desired “low” value of loss $\alpha_{1e}L$ in state 1. For state 2, the same row in the particular table gives an increase $\alpha_{2e} - \alpha_{1e}$ of waveguide propagation loss, generally a “large” increase as desired. Different waveguide geometries in the tables offer flexibility in the magnitude of $\alpha_{2e} - \alpha_{1e}$.

The length L can be on the wavelength-scale if wanted. For the VOA, there is a set of electrically independent, separately addressed GST segments as shown. The electrical drive circuit can turn on some or all of the loss-inducing segments, producing an attenuation that is variable in steps. Speed and power were discussed above.

To give a specific example, the TE mode at 1.55 μ m in Table II offers 0.6 dB of initial loss (the amorphous phase) in an active length of only 2 μ m, and when waveguide length is switched to the crystal phase an attenuation of 14 dB is induced. This expected performance may be compared to a state-of-the-art VOA in SOI silicon photonic devices where 1.55- μ m experiments [31] were conducted on a PIN carrier-injected silicon ridge waveguide having $W \times H$ of 600 nm \times 200 nm. There it was found that a 1000- μ m active length of waveguide produced a nominal zero of attenuation at zero injection, increasing to 30 dB of attenuation at full injection. Comparing the VOA

control power in these two cases, the power is expected to be less in our $L = 2 \mu\text{m}$ self-latching VOA.

Regarding the segmented VOA in Fig. 10(b), there is a question about possible optical losses incurred by unwanted optical reflections at the interfaces between the active and passive waveguide zones. The loss generally is smaller in the amorphous phase where the Si/GST index mismatch is relatively small. The 1×1 of Fig. 10(a) illustrates the basic reflection losses that are then multiplied in (b). Fig. 10(a) is in essence the same as Fig. 1, and there we see the “nominally smooth” end-fire coupling from Si to SGS to Si which actually has interface losses that can be quantified. We performed a finite difference time domain (FDTD) calculation of the unwanted reflection loss in Fig. 1 between a uniform Si channel and the doped SGS channel with its abruptly appearing GST layer in that active segment. Also, a similar FDTD simulation gave us the reflection IL when light entered the output Si channel from the SGS channel. This work was carried out for the amorphous phase. Then calculations were made for the crystalline phase. We turned to Table IV for the SGS parameters at $\lambda = 2100 \text{ nm}$ with $W \times H = 840 \text{ nm} \times 420 \text{ nm}$ and SiO_2 cladding all around. The results of our simulations are as follows $IL(\text{TE}, \text{am}) = 0.075 \text{ dB}$, $IL(\text{TM}, \text{am}) = 0.12 \text{ dB}$, $IL(\text{TE}, \text{cr}) = 1.19 \text{ dB}$ and $IL(\text{TM}, \text{cr}) = 0.17 \text{ dB}$. Each loss just cited is the sum of input and output loss to one GST segment.

IX. CONCLUSION

TE_0 and TM_0 simulations indicate that an ultrathin layer (or layers) of GST embedded in a Si or Ge channel waveguide is viable for SOI-based EO device applications in the near and mid infrared, particularly in spatial routing switches, VOAs, and modulators. Proposals are made for embedding an active EO GST segment within a passive channel waveguide that forms part of a 2×2 or 1×1 device. Simulation results on ER and EA were employed to estimate IL and CT in 2×2 MZIs and 2WGDCs. At $\lambda = 2100 \text{ nm}$, excellent performance is projected for both types of broadband, non-resonant switches. However, at $\lambda = 1550 \text{ nm}$, the IL was “too large”—in the range of 2.3–3.9 dB. If it can be proven that the amorphous GST extinction k remains below 10^{-2} over 2–5 μm wavelengths, then it is likely that high-performance 2×2 switching will be feasible in this domain. For both TE and TM, loss modulation over 1.3–2.1 μm looks feasible with good IL and ER , although the modulator is “binary” with speeds limited to $\sim 1 \text{ Mb/s}$. The VOA is an ideal application for the 1×1 waveguide. By employing independent active regions, a staircase profile of attenuation would be attained as a function of control voltage.

REFERENCES

- [1] H. T. Kim, B. J. Kim, S. Choi, B. G. Chae, Y. W. Lee, T. Driscoll, M. M. Qazilbash, and D. N. Basov, “Electrical oscillations induced by the metal-insulator transition in VO_2 ,” *J. Appl. Phys.*, vol. 107, p. 023702, 2010.
- [2] D. Tanaka, Y. Shoji, M. Kuwahara, X. Wang, K. Kintaka, H. Kawashimi, T. Toyosaki, Y. Ikuma, and H. Tsuda, “Ultra-small self-holding, optical gate switch using $\text{Ge}_2\text{Sb}_2\text{Te}_5$ with a multi-mode Si waveguide,” *Opt. Exp.*, vol. 20 pp. 10283–10294, 2012.
- [3] T. Moriyama, H. Kawashima, M. Kywahara, X. Wang, H. Asakura, and H. Tsuda, “Small-sized Mach-Zehnder interferometer optical switch using

- thin film $\text{Ge}_2\text{Sb}_2\text{Te}_5$ phase-change material,” presented at the Optical Fiber Communication Conference, San Francisco, CA, USA, 2014, Paper Tu3E-4.
- [4] W. H. P. Pernice and H. Bhaskaran, “Photonic non-volatile memories using phase change materials,” *Appl. Phys. Lett.*, vol. 101, p. 171101, 2012.
- [5] P. Hosseini, C. D. Wright, and H. Bhaskaran, “An optoelectronic framework enabled by low-dimensional phase-change films,” *Nature*, vol. 511, pp. 206–211, 2014.
- [6] K. J. A. Ooi, P. Bai, H. S. Chu, and L. K. Ang, “Ultracompact vanadium dioxide dual-mode plasmonic waveguide electroabsorption modulator,” *Nanophotonics*, vol. 2, pp. 13–19, 2013.
- [7] P. Markov, J. D. Rykman, R. E. Marvel, K. A. Hallman, R. F. Haglund, and S. M. Weiss, “Silicon-VO₂ hybrid electro-optic modulator,” presented at the CLEO: Science Innovations, San Jose, CA, USA, 2013, Paper CTu2F-7.
- [8] C. Ye, S. Khan, Z. R. Li, E. Simsek, and V. J. Sorger, “ λ -size ITO and Graphene-based electro-optic modulators on SOI,” *IEEE J. Sel. Topics Quantum Electron.*, vol. 20, no. 4, p. 3400310, Jul./Aug. 2014.
- [9] H. Liang, R. Soref, J. Mu, X. Li, and W. P. Huang, “Long-range mid-infrared propagation in Si and Ge hybrid plasmonic-photon nano-ribbon waveguides,” *Opt. Exp.*, vol. 22, pp. 28489–28499, 2014.
- [10] D. Ielmini, A. L. Lacaita, A. Pirovano, F. Pellizzer, and R. Bez, “Analysis of phase distribution in phase-change nonvolatile memories,” *IEEE Electron Device Lett.*, vol. 25, no. 7, pp. 507–509, Jul. 2004.
- [11] V. Weidenhof, I. Friedrich, S. Ziegler, and M. Wutting, “Laserinduced crystallization of amorphous $\text{Ge}_2\text{Sb}_2\text{Te}_5$ films,” *J. Appl. Phys.*, vol. 89, pp. 3168–3176, 2001.
- [12] V. Weidenhof, N. Pirsch, I. Friedrich, S. Ziegler, and M. Wutting, “Minimum time for laser induced amorphization of $\text{Ge}_2\text{Sb}_2\text{Te}_5$ films,” *J. Appl. Phys.*, vol. 88, pp. 657–664, 2000.
- [13] M. Wuttig and N. Yamada, “Phase-change materials for rewriteable data storage,” *Nature Mater.*, vol. 6, pp. 824–832, 2007.
- [14] W. J. Wang, L. P. Shi, R. Zhao, K. G. Lim, H. K. Lee, T. C. Chong, and Y. H. Wu, “Fast phase transitions induced by picosecond electrical pulses on phase change memory cells,” *Appl. Phys. Lett.*, vol. 93, p. 043121, 2008.
- [15] S. Okamine, S. Hirasawa, M. Terao, and Y. Miyauchi, “Computer simulation of material flow induced by thermal deformation in phase-change recording films,” in *Proc. Appl. Artif. Neural Netw. Int. Soc. Opt. Photon.*, 1992, pp. 315–321.
- [16] R. Soref, “Mid-infrared 2×2 electro-optical switching by silicon and germanium three-waveguide and four-waveguide directional couplers using free-carrier injection,” *Photon. Res.*, vol. 2, pp. 102–110, 2014.
- [17] J. Hendrickson, R. Soref, J. Sweet, and W. Buchwald, “Ultrasensitive silicon photonic-crystal nanobeam electro-optical modulator: design and simulation,” *Opt. Exp.*, vol. 22, pp. 3271–3283, 2014.
- [18] R. Soref, J. Guo, and G. Sun, “Low-energy MOS depletion modulators in silicon-on-insulator micro-donut resonators coupled to bus waveguides,” *Opt. Exp.*, vol. 19, pp. 18122–18134, 2011.
- [19] S. Y. Kim, S. J. Kim, H. Seo, and M. R. Kim, “Variation of the complex refractive indices with Sb-addition in Ge-Sb-Te alloy and their wavelength dependence,” *SPIE Opt. Data Storage*, vol. 3401, pp. 112–115, 1998.
- [20] J. Orava, T. Wagner, J. Sik, J. Pnkryl, M. Frumar, and L. Benes, “Optical properties and phase change transition in $\text{Ge}_2\text{Sb}_2\text{Te}_5$ flash evaporated thin films studied by temperature dependent spectroscopic ellipsometry,” *J. Appl. Phys.*, vol. 104, p. 043523, 2008.
- [21] B. Gholipour, J. Zhang, K. F. MacDonald, D. W. Hewak, and N. I. Zheludev, “An all-optical non-volatile, bidirectional, phase-change meta-switch,” *Adv. Mater.*, vol. 25, pp. 3050–3054, 2013.
- [22] N. Yamada, “Development of materials for third generation optical storage media” in *Phase Change Materials: Science and Applications*, S. Raoux and M. Wuttig, Eds. New York, NY, USA: Springer, 2009, pp. 199–226.
- [23] D. Strand, D. V. Tsu, R. Miller, M. Hennessey, and D. Jablonski, “Optical routers based on ovonic phase change materials,” presented at the Proc. European Phase Change Ovonic Science Symp., Grenoble, France, 2006.
- [24] Y. F. Choi, “Phase-change materials: Trends and prospects,” presented at the ECI Workshop, Lehigh University, Bethlehem, PA, USA, Jan. 10, 2013.
- [25] K. Shportko, S. Kremers, M. Woda, D. Lencer, J. Robertson, and M. Wuttig, “Resonant bonding in crystalline phase-change materials,” *Nature Mater.*, vol. 7, pp. 653–658, 2008.
- [26] H. Tsuda, D. Tanaka, M. Kuwahara, and X. Wang, “Self-holding optical switch using phase-change material for energy efficient photonic network,” presented at the Proc. 24th Symp. Phase Change Oriented Science, Hamamatsu, Japan, 2012, p. A13.

- [27] M. N. Petrovich, F. Poletti, J. P. Wooller, A. M. Heidt, N. K. Baddela, Z. Li, D. R. Gray *et al.*, "Demonstration of amplified data transmission at $2\ \mu\text{m}$ in a low-loss wide bandwidth hollow core photonic bandgap fiber," *Opt. Exp.*, vol. 21, pp. 20559–20569, 2013.
- [28] M. Nedeljkovic, R. A. Soref, and G. Z. Mashanovich, "Free-carrier electrorefraction and electroabsorption modulation predictions for silicon over the 1–14 μm infrared wavelength range," *IEEE Photon. J.*, vol. 3, no. 6, pp. 1171–1180, Dec. 2011.
- [29] C. Huang, R. J. Lamond, S. K. Pickus, Z. R. Li, and V. J. Sorger, "Sub- λ -size modulator beyond the efficiency-loss limit," *IEEE Photon. J.*, vol. 5, no. 4, p. 2202411, Aug. 2013.
- [30] M. Yang, W. M. J. Green, S. Assefa, J. Van Campenhout, B. G. Lee, C. V. Jahnes, F. E. Doany, C. L. Schow, J. A. Kash, and Y. A. Vlasov, "Non-blocking 4x4 electro-optical silicon switch for on-chip photonic networks," *Opt. Exp.*, vol. 19, pp. 47–52, 2010.
- [31] T. Tsuchizawa, K. Yamada, T. Watanabe, S. Park, H. Nishi, R. Kou, H. Shinjima, and S. Itabashi, "Monolithic integration of silicon-, germanium-, and silica-based optical devices for telecommunications applications," *IEEE J. Sel. Topics Quantum Electron.*, vol. 17, no. 3, pp. 516–527, May/Jun. 2011.

Haibo Liang received the B.S. degree from University of Science and Technology of China, Anhui, China, in 2011. He is currently pursuing the Ph.D. degree in the Dept. of Electrical and Computer Engineering McMaster University, ON, Canada.

Richard Soref (S'58–M'63–SM'71–F'03) is currently a Research Professor with the Engineering Program, University of Massachusetts at Boston, Boston, MA, USA. He was a Staff Scientist with the MIT Lincoln Laboratory, Lexington, MA, USA, the Sperry Research Center, Sudbury, MA, USA, and the Air Force Research Laboratory (AFRL), Hanscom AFB, MA, USA. He has been involved in basic research on photonic science and materials physics for the past 50 years, as described in the December 2012 issue of the IEEE PHOTONICS SOCIETY NEWS Magazine. Recent thrusts are in midinfrared photonics and plasmonics. In 1985, he wrote seminal papers on silicon photonics and has been quite active in that field ever since. He co-founded the IEEE International Group IV Photonics Conference in 2004 and later received the Lifetime Achievement Award from that conference. With 52 U.S. patents and many peer-reviewed publications, he has the Google Scholar h-index of 54 along with an i-10 index of 188. For his 27 years as a DoD Scientist, he received the USAF Outstanding Civilian Career Service Award in 2011. Dr. Soref is a fellow of the Optical Society of America, AFRL, and the Institute of Physics, U.K.

Jianwei Mu (M'11) received the Ph.D. degree from McMaster University, Hamilton, Canada in 2011. He is currently working as a research associate in the Electronic Materials (EMAT) group at Massachusetts Institute of Technology. His research interests include nanophotonics, monolithic large scale Mi-IR sensing, ultraviolet detection, chip-scale optical interconnection.

Arka Majumdar is an Assistant Professor jointly in the electrical engineering and physics department in University of Washington, Seattle. He received his B.Tech (H) degree from Indian Institute of Technology, Kharagpur, India in 2007; M.S. from Stanford University in 2009, and Ph.D. from Stanford University in 2012. He worked in University of California Berkeley (2012–13), and in Intel labs (2013–14) as postdoctoral research scientist. His research interests include devices in nanophotonics, nanometallics and quantum optoelectronics with a goal to explore the fundamentals and applications of photonics in information processing. He is the recipient of the Gold Medal from the President of India and the prestigious Stanford Graduate Fellowship among other accolades.

Xun Li (M'93–SM'04) received the B.S., M.S., and Ph.D. degrees from Shandong University, Jinan, Wuhan Research Institute of Posts Telecommunications, Wuhan, and Beijing Jiaotong University, Beijing, all in China, in 1982, 1984, and 1988, respectively. He joined the Department of Electrical and Computer Engineering at McMaster University, Hamilton, ON, Canada in 1999 as an Assistant Professor, where he became an Associate Professor in 2003, and a Professor in 2008. He has authored and co-authored over 250 journal and conference papers. He has also authored a book and a book chapter on optoelectronic device modeling and simulation. He is an adjunct professor with Beijing Jiaotong University and Huazhong University of Science and Technology.

Dr. Li is a member of OSA, SPIE, and a licensed Professional Engineer of Ontario, Canada.

Wei-Ping Huang (M'88–SM'96) received the Ph.D. degree from the Massachusetts Institute of Technology (MIT), Cambridge, in 1989, in electrical engineering with major in photonics. He is currently the Dean and a Professor with the School of Information Science and Engineering, Shandong University, Jinan, Shandong, China. He is internationally known for his contributions and expertise for photonic devices and integrated circuits, especially in the computer-aided design technologies for photonic devices and ICs. He has authored and coauthored over 140 journal papers and 70 conference papers and holds seven U.S. patents. Dr. Huang is a member of OSA and a member of the MIT Electromagnetics Academy. He was elected as a Cheung Kong Scholar by the Ministry of Education, People's Republic of China, and Li Ka Shing Foundation, Hong Kong, in 2000.